Recombination and enhanced metastable repopulation in the argon afterglow

Yusuf Celik,[1] Tsanko V. Tsankov,[1,*] Mitsutoshi Aramaki,[2] Shinji Yoshimura,[3] Dirk Luggenhölscher,[1] and Uwe Czarnetzki[1]

[1]*Institute for Plasma and Atomic Physics, Ruhr University Bochum, 44780 Bochum, Germany*

[2]*Department of Electrical Engineering and Computer Science, Nagoya University, Nagoya 464-8603, Japan*

[3]*National Institute for Fusion Science, Toki 509-5292, Japan*

(Received 2 March 2012; published 8 May 2012)

The power-off phase of pulsed low-pressure plasmas (the so-called afterglow) in noble gases is a rich field for both fundamental and application oriented research. The physics of these plasmas is complex and involves various processes: Initially, electrons cool rapidly to temperatures close to the gas temperature by evaporative cooling. At sufficiently high plasma densities the low kinetic electron energy strongly enhances three-body recombination into Rydberg states. Finally, subsequent collisional-radiative decay leads to emission of radiation and populates the metastable states of the atoms. The various steps are investigated experimentally and are compared to analytical models. This allows us to follow all steps throughout in a single experiment involving diagnostics of electron density, metastable density, and emission. Excellent agreement with the models is achieved. The mechanisms included are: (i) for electrons, balance between evaporative cooling and Coulomb collisions with ions leading to thermalization; (ii) consistent combination of re-ionization and microfield reduction of the ionization energy in the recombination rate; (iii) adiabatic balance of recombination and collisional and radiative de-excitation; and (iv) radiative population and diffusional and pooling collisional loss of metastable levels. Although the experiment is carried out in argon, the underlying physics is generally applicable for the afterglow of high-density low-pressure discharges in atomic gases.

DOI: 10.1103/PhysRevE.85.056401 PACS number(s): 52.25.−b, 52.38.Dx, 52.70.Kz, 52.80.Pi

I. INTRODUCTION

Decaying plasmas without external energy supply exhibit some unique properties with rather complex dynamical relation between electron heating and cooling mechanisms coupled to particle transport, recombination, and re-ionization processes. At low temperatures and in particular in noble gases the dominant loss channel for the electron energy is evaporative (diffusive) cooling.

This highly efficient cooling mechanism was first observed by Biondi [1] and since then several investigations, both theoretical and experimental, have been devoted to this effect [2–6]. Although the general mechanisms behind the process are clear, a satisfactory quantitative agreement between theory and experiment was lacking. Recently [7], an *ab initio* analytical model was able to fully reproduce the experimental and simulation results, thus providing a satisfactory quantitative description of the electron cooling process.

The decrease of the electron temperature through evaporative cooling quickly extinguishes all excitation processes. The low-electron energy in combination with sufficiently high-electron densities, however, strongly enhance recombination. Although various recombination mechanisms exist at low pressure and in atomic gases, three-body recombination (TBR) is by far the dominant process [8–11]. The rate for this process, $\nu_{\mathrm{TBR}} = -(1/n_e)(\partial n_e/\partial t)$, is commonly cited to scale as $n_e^2 T_e^{-4.5}$ [12]. This is the scaling first obtained by Thomson [13] using a cut off for the re-ionization by thermal electrons as the limiting factor for the recombination rate. Later this result had been confirmed by detailed collisional radiative models for hydrogen [14,15]. The calculations of Stevefelt *et al.* [16] provided some additional correction terms to the rate. Pohl *et al.* [17] showed recently that the rates used in the calculation of Stevefelt *et al.* are incorrect for transitions between states with energy difference smaller than $0.5kT_e$. These authors also developed a collisional radiative model where they used the Stark splitting by plasma microfields as a factor limiting the recombination. The effect of plasma microfields on the recombination rate has been investigated by Hahn [18]. In his approach the effect of the microfields and the re-ionization by thermal electrons are treated as independent competing processes.

Three-body recombination populates predominantly the states close to the ionization continuum, the so-called highly excited Rydberg states [19]. The standard physical picture of the atomic population dynamics after recombination distinguishes between two groups of bound states [14–17]. For upper Rydberg states between the ionization limit and a lower "bottleneck" state, collisional de-excitation dominates. Below the bottleneck state, radiative de-excitation is dominant and at the critical state both rates are equal. The radiative transitions give rise to emission of photons, occurring after power termination, where the name "afterglow" comes from. This afterglow was observed already in the 1950s by Johnson *et al.* [20] and was subject to numerous subsequent studies.

The collisional-radiative de-excitation of the recombined Rydberg atoms leads eventually to repopulation of the metastable states. It is known that these states play a crucial role in the afterglow of noble gas plasmas [21–25]. As long-lived species they can store a significant amount of energy. Such excited species can influence the shape of the electron energy distribution function [26] or reheat the electrons and modify the properties of the afterglow [27,28].

In this work an attempt is made to determine in a single experiment the relevant parameters belonging to the various processes outlined above. In particular the electron density, the optical emission, and the metastable density are measured

*tsanko.tsankov@rub.de

using various diagnostics and are combined in a single consistent picture by analytical models. Furthermore, a model is proposed which combines re-ionization and microfield limited recombination with electron evaporative cooling and heating by Coulomb collisions with ions. Good agreement with measurements in an argon discharge is obtained. However, the basic properties determining the system dynamics are independent of the particular atomic species. Therefore, the physics investigated in this paper should apply to any atomic system as long as evaporative cooling and three-body recombination of electrons are dominant mechanisms in the afterglow. At higher pressures electron-molecular ion recombination and electron energy loss by elastic collisions may eventually become important, a regime explicitly excluded here.

The outline of the paper is as follows: First the theoretical models are introduced, then the experiment is described, and finally the experimental data are compared to the theory. The paper closes with a section summarizing the conclusions drawn from the results. Some more specific details of the discussion are moved to an Appendix.

II. THEORY

This section presents the analytical models, describing the temporal evolution of different plasma parameters in the various stages of the afterglow. The models are interconnected and present a consistent picture of the processes in the afterglow. The general physical picture of the afterglow is outlined in Fig. 1.

After the external power is cut, a short transient period (few microseconds) follows during which the electrons with energy above the excitation threshold (11.48 eV) lose energy by inelastic collisions and the excited species present during the active phase of the discharge decay radiatively. Subsequently the electron energy continues to decrease through evaporative (diffusive) cooling. This phase lasting about 1 ms (depending on pressure and chamber size) is described in Ref. [7]. Simultaneously with the electron energy decay, quenching of the metastables takes place. When the electron temperature reaches values around room temperature (0.026 eV), the recombination phase begins. Furthermore, quenching of metastables effectively terminates as the electron temperature has fallen significantly below the energy required for excitation from the metastable to the resonant state (0.076 eV). Three-body recombination, dominant at low pressures, populates the higher Rydberg states. These states relax through the bottleneck by electron collisions to lower radiative states. The radiative states then further relax downward by emission of photons and end up either in a metastable state or in the ground state. The metastable states finally are lost by diffusion to the walls and energy pooling. A simplified system of atomic levels is considered in the models (Fig. 1).

A. General recombination rate

Following the classical approach of Thomson [13,29] one obtains an expression for the ionization coefficient of an atom in an excited state characterized by a quantum number p and density n_p. Combining this coefficient with the Saha formula and the principle of detailed balancing the following recombination coefficient α_p ($\dot{n}_p = \alpha_p n_e^2 n_i$) into the state p is obtained:

$$\alpha_p = \frac{4}{\pi}\frac{h^3 a_0^2}{m_e^2}\left(\frac{g_p}{g_e g_i}\right)\left(\frac{R_y}{I_p}\right)^2 \frac{\Gamma_p}{kT_e}. \tag{1}$$

Here a_0 is the Bohr radius, $R_y = 13.6$ eV the Rydberg energy, I_p and g_p are the ionization energy and the statistical weight of the atomic state, g_e and g_i are the statistical weights of the recombining electron and ion, respectively, Γ_p is the Gaunt factor, and T_e the electron temperature. The other notations are standard. Setting $g_e = 2$, $g_i = 4$ ($j = 3/2$) and $g_p = 8p^2$ (the atom consists of the ionic core and an electron in an outer orbital), as well as taking $\Gamma_p = 1$, Eq. (1) has the form

$$\alpha_p = C\left(\frac{R_y}{I_p}\right)^2 \frac{p^2}{T_e}. \tag{2}$$

The constant $C = 4h^3 a_0^2/(\pi m_e^2 k)$ has the value of $C = 9.05 \times 10^{-38}$ m^6 K s^{-1} $= 7.80 \times 10^{-42}$ m^6 eV s^{-1}. It has to be noted

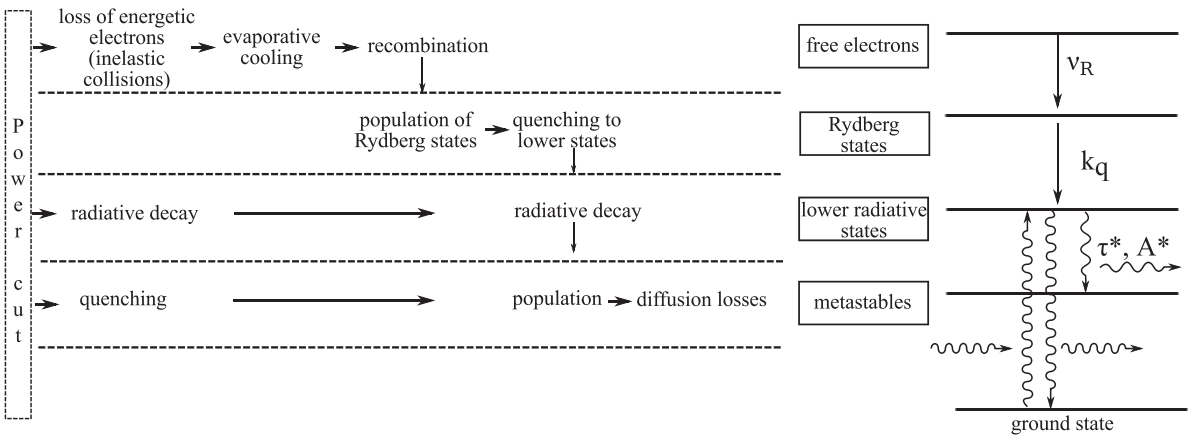

FIG. 1. A schematic representation of the interconnection of the different physical processes occurring in the afterglow of noble gas plasmas. For the sake of simplicity some processes are not included. For example, the diffusional losses of electrons occurring during the entire afterglow and the energy pooling of metastables, of importance at higher pressures, are omitted. The simplified level scheme assumed in the analytical models is also given.

that a formula similar to Eq. (1) and (2) is given also by Hahn [18,30], but the value of the numerical coefficient is different probably due to an error in the conversion of units. This error then spreads into a paper by Killian *et al*. [19].

Using the Balmer formula for the ionization energy $I_p = E_i/p^2$ with E_i the ionization energy of the atom (argon in the case studied here) Eq. (2) becomes

$$\alpha_p = C\left(\frac{R_y}{E_i}\right)^2 \frac{p^6}{T_e} = C' \frac{p^6}{T_e} \tag{3}$$

with $C' = C(R_y/E_i)^2 = 6.74 \times 10^{-38}$ m^6 K s^{-1} $= 5.81 \times 10^{-42}$ m^6 eV s^{-1} for argon. This formula shows that the three-body recombination populates predominantly the higher lying states since the rate for their population scales with the principle quantum number like p^6 [19]. Strictly speaking, the Balmer formula applies only to hydrogen and in noble gases the quantum defect formula for the energy of the eigenstates [31] might be more appropriate. As will be shown, the Balmer formula gives already remarkable agreement with experiments.

The net recombination rate ν_r for electrons is calculated by summing the population rate α_p of all states up to a maximum quantum number p_m. This maximum quantum number is determined by ionization by thermal electrons and microfields in the plasma, to which the Rydberg states are rather sensitive. This has been discussed, for example, in Refs. [18,32]. For sufficiently high values of this maximum number the finite sum can be replaced by an integral:

$$\begin{aligned}\nu_r = n_e^2 \sum_{p=1}^{p_m} \alpha_p &= \frac{C'}{T_e} n_e^2 \sum_{p=1}^{p_m} p^6 \\ &\approx \frac{C'}{T_e} n_e^2 \int_1^{p_m} p^6 dp \approx \frac{C'}{7T_e} n_e^2 p_m^7.\end{aligned} \tag{4}$$

If as the maximal quantum number the Thomson value is taken ($p_m = \sqrt{E_i/kT_e}$), the well-known scaling of the recombination rate is obtained:

$$\nu_r = A \frac{n_e^2}{T_e^{9/2}}. \tag{5}$$

The physical meaning of this cut-off criterium is that all states within one kT_e from the continuum are ionized by thermal electrons and do not contribute to the recombination. In Eq. (5) the constant A has the value 2.52×10^{-20} m^6 K$^{9/2}$ s^{-1} $= 1.29 \times 10^{-38}$ m^6 eV$^{9/2}$ s^{-1} for argon.

As an alternative cut-off mechanism one can take the plasma microfields, as proposed by Hahn [18]. In this case the maximum quantum number is given by the well-known Inglis-Teller formula [33]:

$$p_m = \left(\frac{n_{IT}}{n_e}\right)^{2/15}, \tag{6}$$

where $n_{IT} = 10^{29.19}$ m^{-3} is the scaling density resulting from the Inglis-Teller formula. At this density, the Stark effect would hypothetically not allow any bound state. The value used here is the corrected one by Mitrofanov [34] for an error in the mean Holtsmark field in the original work [33]. The physical picture behind the formula is that the ionic microfield is leading to a mean Stark splitting of all states. For p larger than the maximum quantum number, the Stark splitting of the state p is already larger than the energy difference to the state $p+1$ so that effectively the transition to the continuum appears already at a finite quantum number. As a result the ionization potential in plasmas is effectively lowered. With p_m from Eq. (6) the recombination rate takes the form

$$\nu_r = C' \frac{n_{IT}^{14/15}}{7T_e} n_e^{16/15}. \tag{7}$$

These commonly utilized derivations suffer from the following misconception. The re-ionization by thermal electrons is not a process competing with the microfield effect, but rather a complementary one. This means that the limiting quantum number has to be determined from the following expression:

$$\frac{E_i}{p_m^2} = \frac{E_i}{p_{IT}^2} + \eta k T_e. \tag{8}$$

Here p_{IT} is given by Eq. (6). The first term on the right-hand side (rhs) in Eq. (8) describes the lowering of the ionization potential and the second term gives the additional limitation of the maximal quantum number due to re-ionization by thermal electrons. The position of the bottleneck is accounted for by the dimensionless parameter η. Its value varies between different authors which is probably the cause for the different magnitudes of the recombination rates cited. For example, the original formulation of Thomson corresponds to $\eta = 1$ and the calculations by Pohl *et al*. provide $\eta \approx 4$. Combining (8) with (4) the following recombination rate formula is obtained:

$$\nu_r = -\frac{1}{n_e}\frac{\partial n_e}{\partial t} = \frac{C' E_i^{7/2}}{7\eta^{7/2}} \frac{n_e^2}{T_e^{9/2}} \frac{1}{(1+\psi_{IT})^{7/2}}, \tag{9}$$

with

$$\psi_{IT} = \frac{E_i}{\eta k T_e p_{IT}^2} = \frac{E_i}{n_{IT}^{4/15}} \frac{n_e^{4/15}}{\eta k T_e}. \tag{10}$$

Equation (9) gives a smooth transition between the standard $T_e^{-4.5}$-rate formula (5) and the one given by Eq. (7). Both formulas are recovered in the limiting cases of, respectively, $\psi_{IT} \ll 1$ and $\psi_{IT} \gg 1$.

B. Influence of the evaporative cooling

In a recent work [7] a general description of the evaporative cooling was achieved. It was shown that the electron dynamics in the afterglow can be divided into two phases: before and after the electron temperature has reached the gas temperature. Initially, when the electron temperature T_e is higher than the gas temperature T_g electrons lose energy at a rate greater than the particle loss rate. During this phase diffusive losses with a temporally varying diffusion coefficient determine the electron density $n(\tau)$ evolution:

$$n = \left(\frac{\beta}{(1+\beta)e^{\beta\tau} - 1}\right)^{\gamma}. \tag{11}$$

Here $\tau = t/\tau_\varepsilon$ with τ_ε denoting the electron energy decay time due to evaporative cooling. The electron density n is normalized to its initial value $n_e^{(0)}$. The parameter β is the ratio of the gas temperature T_g to the initial electron temperature

$T_e^{(0)}$, both have been measured in Ref. [35]. The parameter γ is given by the ratio of τ_ε to the steady-state diffusion time $\tau_D^{(0)}$.

The electron temperature reaches the gas temperature at a time $t = t_\beta \approx \tau_\epsilon(T_e^{(0)}/T_g)$. The electron density at this time is $n_e(t = t_\beta) = n_\beta = n_e^{(0)}(T_g/T_e^{(0)})^\gamma$.

At later times, after thermalization, Coulomb collisions of electrons with ions start to dominate. As a result, the electron temperature changes adiabatically which connects the electron temperature with the density. Numerical simulations show that this relation has a surprisingly simple power scaling that holds in a large interval of electron temperatures [7]:

$$kT_e = \delta n_e^{2/5} = \delta n_e^\kappa, \quad \kappa = 2/5. \tag{12}$$

The coupled equations of temperature decay by diffusional transport and heating by Coulomb collisions and particle loss by diffusion and recombination are complex and not treatable analytically. However, the above relation might be motivated by the following considerations. With adiabatic change of the electron temperature and balance between electron heating by Coulomb collisions with the ions and cooling by evaporative the following equation is obtained:

$$kT_e(kT_e + kT_g) = \alpha_0 \frac{n_e}{(kT_e)^{3/2}}(kT_g - kT_e). \tag{13}$$

Here the ion temperature is assumed to be equal to T_g and the constant α_0 is

$$\alpha_0 = \sqrt{\frac{m_e}{2\pi}} \frac{e^4}{384\epsilon_0^2} \frac{L^2 \nu_{in} \ln \Lambda}{\ln[L v_{th}/(16 D_a)] + 2}. \tag{14}$$

In this equation ν_{in} is the ion-neutral elastic collision frequency, $\ln \Lambda \approx 6$ is the Coulomb logarithm, L is a characteristic length of the plasma chamber, and D_a and v_{th} are the ambipolar diffusion coefficient and the electron thermal velocity at gas temperature. The n_e-T_e relation given by Eq. (13) cannot be inverted exactly to obtain the temperature as a function of the density. Rearranging Eq. (13) yields

$$kT_e = \delta(T_e) n_e^{2/5} \approx \alpha_0^{2/5} n_e^{2/5}, \tag{15}$$

$$\delta = \alpha_0^{2/5} \left(\frac{T_g - T_e}{T_g + T_e}\right)^{2/5}. \tag{16}$$

Expression (12) follows in the limit $T_e \ll T_g$ with $\delta = \alpha_0^{2/5}$. For finite values of T_e Eq. (12) can still be considered to hold with $\delta(T_e)$ being a slowly varying function of the temperature or, respectively, the density. Apparently $\delta(T_e = T_g) = 0$. In fact, the electron temperature has to be below the gas temperature in all cases to realize the adiabatic balance. Therefore, one can expect $\delta < \alpha_0^{2/5}$.

By combining (12) with (9) the following rate formula is obtained:

$$\nu_r = \frac{C' E_i^{7/2}}{7\eta^{7/2}} \frac{n_e^2}{\left(\delta n_e^{2/5}\right)^{9/2}} \frac{1}{(1 + \hat{\psi}_{IT})^{7/2}} = \rho \frac{n_e^{1/5}}{(1 + \hat{\psi}_{IT})^{7/2}}, \tag{17}$$

$$\rho = \frac{C' E_i^{7/2}}{7\eta^{7/2}\delta^{9/2}}, \tag{18}$$

$$\hat{\psi}_{IT} = \frac{E_i}{\eta \delta n_{IT}^{4/15}} \frac{1}{n_e^{2/15}}. \tag{19}$$

At high densities in the limit $\hat{\psi}_{IT} \ll 1$ Eq. (17) shows that the recombination rate should exhibit a $n_e^{1/5}$ dependence with the density. In the other limiting case of low electron densities $\hat{\psi}_{IT} \gg 1$ the recombination rate shows a stronger $n_e^{2/3}$ variation. For the experimental conditions considered here the high-density case ($\hat{\psi}_{IT} \approx 0.1 \ll 1$) applies. Therefore in the following theoretical treatment the recombination rate will be considered to scale as $n_e^{1/5}$. This leads to a reasonable agreement with the experiment.

C. Evolution of the electron density

At low pressures the charged particles are lost by recombination and diffusion, no ionization occurs. At high electron densities and low electron temperatures (after thermalization) the diffusion can be neglected. In this case

$$\dot{n}_e = -\nu_r n_e = -\rho n_e^{6/5}, \tag{20}$$

where ν_r is given by Eq. (17). The solution to this equation with the initial condition $n_e(t = t_\beta) = n_\beta$ is

$$n_e(t) = \frac{n_\beta}{\left[1 + (1/5)\rho n_\beta^{1/5}(t - t_\beta)\right]^5}. \tag{21}$$

Here it is assumed that the time t_β when thermalization is achieved also marks the transition between the initial cooling phase and the following recombination phase. The solution (21) does not depend on the initial density n_β for $t \to \infty$. This property is typical for all recombination dominated discharges. It should be noted further that the temporal evolution of the density is not very sensitive to the exact power dependence of the recombination rate on n_e as long as this dependence is weak (see the Appendix).

D. Excited states dynamics

The following states of the argon atom are considered (cf. Fig. 1): the Rydberg levels n_R above the bottleneck, the excited levels n^* below the bottleneck, and the metastable states n_m. The Rydberg levels are populated by recombination and lost due to electron-impact quenching (with a rate constant k_q):

$$\dot{n}_R = \nu_r n_e - k_q n_e n_R. \tag{22}$$

The excited radiative states are then populated from the Rydberg states and lost due to spontaneous emission (with a lifetime τ^*):

$$\dot{n}^* = k_q n_e n_R - n^*/\tau^*. \tag{23}$$

The radiative and quenching rates (by electron collisions) as a function of the principal quantum number p are shown in Fig. 2. The rates are calculated using standard formulas [36,37]. The electron density range covered in the experiment is represented by the curves for quenching. From this graph one expects the bottleneck between $p = 12$ and 21, depending on the electron density.

The metastable states are populated from the radiative states (with a probability A^*) and lost by diffusion (with a diffusive time constant τ_D) and energy pooling (with a rate constant k_m):

$$\dot{n}_m = A^* n^* - n_m/\tau_D - 2k_m n_m^2. \tag{24}$$

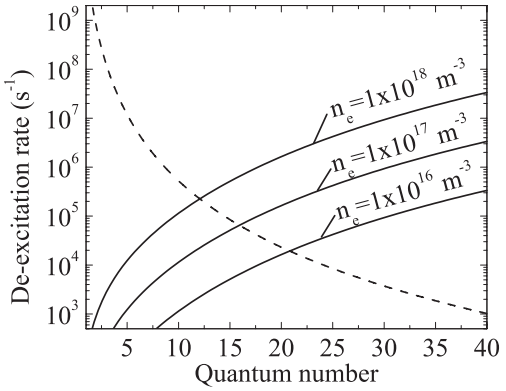

FIG. 2. Radiative (dashed curve) and quenching (continuous curves) de-excitation rates as function of the principal quantum number. The quenching rates are calculated for different electron densities and an electron temperature equal to the gas temperature.

It can be assumed that the densities of the Rydberg states above the bottleneck and of the excited radiative states are limited by their losses, that is, they are changing adiabatically ($\dot{n}_R \approx 0, \dot{n}^* \approx 0$). In this case their densities are

$$n_R(t) \approx \frac{\nu_r}{k_q} = \frac{\rho}{k_q} \frac{n_\beta^{1/5}}{\left[1 + (1/5)\,\rho n_\beta^{1/5}(t - t_\beta)\right]}, \quad (25)$$

$$n^*(t) \approx k_q \tau^* n_e n_R = \frac{\rho \tau^* n_\beta^{6/5}}{\left[1 + (1/5)\,\rho n_\beta^{1/5}(t - t_\beta)\right]^6}. \quad (26)$$

In the experiment the intensity of the emitted light is observed: $I \propto n^*$. It has the same temporal variation as the population density of the emitting states.

For the metastable states the loss mechanisms are much slower than the population and quasisteady state cannot be assumed for them. At lower pressures the metastable densities in the afterglow are low (due to less recombination) and the diffusional losses dominate over energy pooling. In this case, assuming that at the end of the cooling phase of the electrons the metastables are completely quenched, the solution of Eq. (24) is

$$n_m(t) = A^* \tau^* \rho n_\beta^{6/5} \exp\left(-\frac{t}{\tau_D}\right) \times \int_{t_\beta}^{t} \frac{\exp(t'/\tau_D)}{\left[1 + (1/5)\rho n_\beta^{1/5}(t' - t_\beta)\right]^6} dt'. \quad (27)$$

Here $A^*\tau^*$ is the branching ratio of excited state(s) for radiative transitions to the metastable state. In fact, the diffusive losses of the metastables are so slow in comparison with the density variation that the exponent under the integral can be taken as unity. This allows the integration to be performed yielding

$$n_m(t) \approx A^* \tau^* n_\beta \exp\left(-\frac{t}{\tau_D}\right) \times \left\{1 - \frac{1}{\left[1 + (1/5)\rho n_\beta^{1/5}(t - t_\beta)\right]^5}\right\}. \quad (28)$$

At higher pressures, owing to higher plasma densities, the recombination process is more pronounced. As a result the metastable density in the afterglow is higher, in some cases even exceeding the steady-state value. In this case the energy pooling is comparable to the diffusional losses and cannot be neglected. This does not permit an analytical solution to Eq. (24). However, an approximate solution can still be found due to the different time scales of the terms in the equation. The first term on the rhs of Eq. (24) has a strong time variation given by Eq. (26). It describes the rise in the metastable density after the end of the quenching phase and quickly diminishes. In the subsequent decay of the metastables this term is small and can be neglected. With this approximation and the initial condition $n_m(t = t_{max}) = n_{max} = A^*\tau^* n_\beta$, where n_{max} is the peak density of the metastables reached in the afterglow at time t_{max}, the solution is

$$n_m(t) \approx \frac{n_{max}}{(1 + 2k_m \tau_D n_{max}) \exp\left[(t - t_{max})/\tau_D\right] - 2k_m \tau_D n_{max}}. \quad (29)$$

The derived formulas describe the general temporal evolution of the different plasma parameters in the low pressure afterglow. In the next sections these predictions will be compared against experiments. The comparison is mainly in the form of fits of the corresponding equations to the experimental data. The lack of knowledge on certain quantities, like for example, the branching ratio for populating the metastables, entering the theoretical formulas does not allow calculating all quantities *ab initio*. However, these factors concern mostly the absolute scaling and not the time constants and the actual functional dependence given by the equations.

III. EXPERIMENTAL SETUP

A schematic of the discharge chamber and the adherent diagnostics is given in Fig. 3. The plasma is produced by radio-frequency (rf) power at $f_{rf} = 13.56$ MHz coupled via a 2.5 turn fourfold inductive planar antenna (200 mm diameter) [35,38]. The antenna is separated from the plasma by a quartz dome of 12 mm thickness. All measurements are performed in the downstream plane 240 mm below the quartz dome in

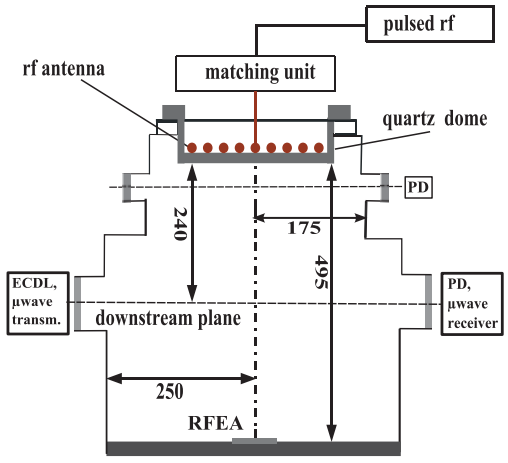

FIG. 3. (Color online) Schematic of the experimental setup. The dimensions are in millimeters and the notations used are the following: ECDL (external cavity diode laser), PD (photodiode), and RFEA (retarding field energy analyzer).

an argon plasma. The rf power to the antenna is supplied by a Dressler Cesar 1312 rf generator through a standard L-type matching unit (VM 1000). In the experiment the reflected power is zero under all conditions and power values given below refer to the output of the generator. The rf power is pulsed with a duty cycle of 85% at a repetition frequency of 20 Hz, but depending on the conditions 5 and 10 Hz are also used. The fall time of the rf current in the generator amounts to less than 1 μs.

The time-resolved line-integrated electron density is measured by means of a microwave interferometer (MWI) [39]. This technique has the advantage of being noninvasive but only the line averaged densities can be obtained. A cosine profile is assumed to convert the measured densities to the values in the center. A rough estimation shows that the possible error caused by deviation of the profile due to recombination is not larger than about 10%. The linear frequency f of the interferometer (Miwitron Ltd., MWI 2650) is 26.5 GHz. A pair of lenses located in front of the emitter and the receiver (separated by about 2 m) is used to increase the signal to noise ratio. The time resolution of the system is 10 μs and the minimum measurable electron density is about 10^{14} m^{-3}.

To cover the whole dynamic of the density decay, the repetition rate of the rf pulse is set to 5 Hz. The curves measured with an oscilloscope (LeCroy WaveSurfer 424) consist initially of 250 000 points. The data are numerically processed: 100 points corresponding to an interval of 20 μs are averaged to produce a single data point. The reduced data set is then numerically differentiated by using a Savitzky-Golay filter with an adaptive control of the window size [40]. This ensures a reasonable trade-off between temporal resolution and additional filtering.

The plasma emission in the afterglow is recorded by using a Hamamatsu photomultiplier tube (R 928). A tunable interference filter (VariSpec VIS) with a full width at half maximum (FWHM) of 10 nm is adjusted to a wavelength of 418 nm. Thus, line-integrated emission in the wavelength range between 413 and 423 nm is recorded. Additionally, a 1/8 m grating spectrometer (Oriel) in combination with an intensified CCD camera (Roper PIMAX) is used to record time-resolved spectra in the afterglow. The spectrograph consists of an entrance slit of 200 μm, two parabola mirrors with a focal length of 125 mm, and a grating with a line density of 400 grooves/mm. A mechanical micrometer drive controls the wavelength tuning. The wavelength resolution of this system is about 1.6 nm and the wavelength range is about 250 nm. The absolute frequency calibration is done by use of two sufficiently isolated and identifiable plasma emission lines. Plasma light is collected by an optical fiber of 200 μm diameter and a numerical aperture 0.22 which guides the light to the input slit of the spectrometer.

The temporal evolution of the line averaged metastable density is measured by a tunable diode laser absorption spectroscopy (TDLAS) system. It consists of a compact grating-stabilized external cavity diode laser (ECDL) [41] and the adherent optics. The laser is tuned at 696.73 nm corresponding to the $2p_2 \leftarrow 1s_5$ Ar atom transition (in Paschen notation). Wavelength monitoring is done via a Fabry-Pérot interferometer. To avoid saturation, the laser power is reduced to about 3 μW via a neutral density filter. The laser beam transmission behind the plasma is detected via an ultrafast Si PIN photodiode (PD, EG&G FND 100, rise time < 1 ns). To increase the signal to noise ratio, a 10 kΩ terminal resistance is chosen, leading to an effective time resolution of around 1 μs. An interference filter (FWHM $= 10$ nm) is installed in front of the detector. The measurements at 1 Pa were performed at a repetition frequency of 20 Hz, but at higher pressures this is reduced to 10 Hz to cover the whole dynamics of the metastables.

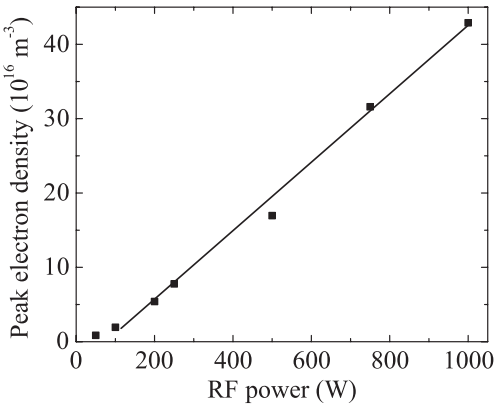

FIG. 4. Variation of the steady-state center density with power at a pressure of 1 Pa measured by microwave interferometry.

A 3-grid retarding field energy analyzer (Impedans Semion) placed at the bottom of the chamber is combined with a digital oscilloscope (LeCroy WaveSurfer 424) to record temporally resolved ion energy distributions. Via the floating potential their peak energy is converted into temporally resolved electron temperatures. Comparison between measured and calculated values is made in a recent paper [7].

IV. EXPERIMENTAL RESULTS

In this section the results from the various experimental techniques employed are presented. The different aspects of the recombination are investigated and a comparison with the theoretical formulas is shown.

A. Electron density evolution

Figure 4 shows the dependence of the center plasma density on the rf power in the stationary discharge in argon at 1 Pa. An almost linear increase with the power is observed as expected [12]. These densities are identical to the initial values for the density decay in the afterglow (shown in Fig. 5) since the duty cycle is large. In the afterglow the temporal evolution at lower powers and hence lower initial plasma densities is fundamentally different from the one observed at higher initial densities—the higher the density, the faster the decrease. This dependence on the initial density can be easily understood in terms of recombination in the plasma volume—at higher densities the charged particles are lost due to recombination in addition to the diffusive losses, which leads to the steeper slope. Furthermore, three different decay intervals can be identified in Fig. 5—an initial fast decrease in the first 1–2 ms, an almost exponential interval until around 12 ms, immediately followed

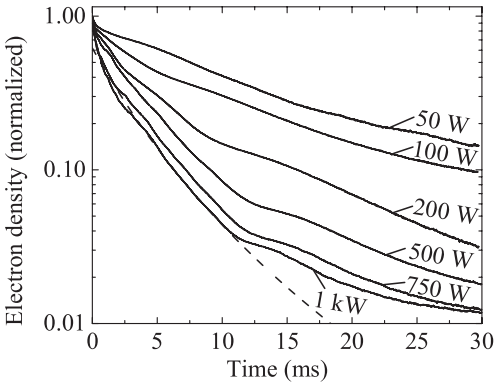

FIG. 5. Temporal development of the electron density normalized to its initial value as a function of power at $p = 1$ Pa. The dashed curve represents a fit to the data at 1 kW according to Eq. (21).

by an interval of slower density decrease during the rest of the afterglow phase.

The initial density decay phase is well described by ambipolar diffusion with a temporally changing electron temperature due to the evaporative cooling. The electron density variation is given in this case by Eq. (11). Figure 6 shows the measured electron density for one of the curves in Fig. 5 (50 W) in this initial time interval with a fit according to Eq. (11) superimposed. The agreement between measurement and model is excellent and this is also the case at other powers [7]. The values of the fit parameters are also close to those predicted by the theory. Similarly, good agreement is also found for the electron temperature decay [7].

The second interval, starting at about 2 ms and continuing to roughly 12 ms after pulse termination, shows a qualitatively different behavior—different slopes at different powers are observed. In this time interval the electron temperature has reached gas temperature and recombination has been triggered. This is confirmed by the good agreement of Eq. (21) with the data for the case of 1 kW (Fig. 5). The different slopes at different powers are due to different values of the density n_β at the beginning of the recombination phase. Between 50 W and 1 kW clearly the density decay makes a transition from the diffusion to the recombination dominated regime.

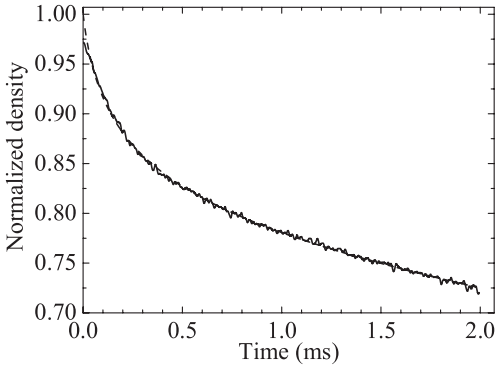

FIG. 6. Measured electron density decay for 50 W at $p = 1$ Pa obtained with the microwave interferometer. A fit of Eq. (11) is superimposed (dashed curve). The fit results provide $\beta = 0.028$, $\gamma = 0.07$, and $\tau_\epsilon = 42\ \mu$s, in good agreement with the model [7].

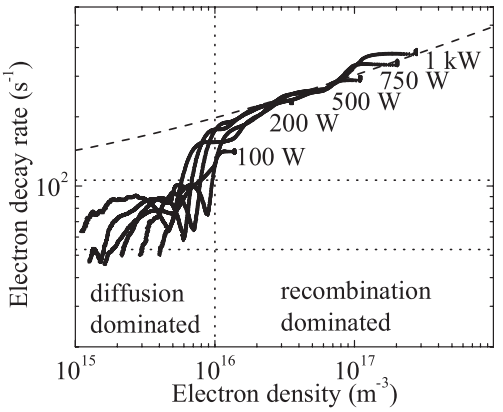

FIG. 7. Decay rates of the plasma density obtained from the MWI measurements at 1 Pa and different powers. The horizontal dotted lines present the diffusional loss rate at $T_e = 0$ (lower line) and at $T_e = T_g$ (upper line). The dashed curve gives the prediction of the theoretical formula (17) with $\eta = 1$ plus a diffusional rate at $T_e = 0.8T_g$ (see text for explanations).

The last and final phase in the electron density evolution, which spans from about 12 ms until the end of the afterglow, is determined by a pure diffusional decay. Although at higher power levels, that is, at higher steady-state electron densities, considerable gas heating takes place (as measured in Ref. [35]), analytical estimations show that the gas temperature reaches room temperature on a time scale of about 3 ms. This has an influence only on the first phase, while during the second and third intervals diffusion takes place at room temperature. Therefore the diffusional electron loss rate is the same for all powers leading to identical slopes exhibited in the third and final phase of the electron decay.

From the curves in Fig. 5 the electron decay rates are obtained and plotted against the density (Fig. 7). Apparently all curves overlap and follow the same slope. At lower densities (the third phase in the decay) all curves converge in the ambipolar diffusion regime, as expected. The actual diffusion rates vary for each case but are confined between the values corresponding to zero electron temperature and an electron temperature equal to the ion temperature (considered to be equal to the gas temperature). It should be noted that in this region of low densities and rates noise, especially resulting from differentiation, is rather large.

The slope on the right goes with the power of 0.2. Here the factor $\hat{\psi}_{IT}$ in Eq. (17) has only a very low value close to 0.1 and, hence, has a relatively small contribution. In such case Eq. (17) predicts exactly the same density scaling. For comparison, the Hahn formula (7) gives a much steeper $n_e^{2/3}$ dependence which is clearly well outside the uncertainty limits of the experimental data. This means that the maximum quantum number is limited mainly by re-ionization by thermal electrons and to a much lesser extent by microfields [in Eq. (8) the second term on the rhs dominates over the first one].

The exact prediction of Eq. (17) (with an added constant diffusional rate) is also shown in Fig. 7. It has to be noted that for a good quantitative agreement the value of δ in Eq. (12) is $0.42\alpha_0^{2/5}$. This corresponds in the frame of the reasoning given for δ to an electron temperature of $T_e \approx 0.8T_g$ for $\eta = 1$ and

$T_e \approx 0.99 T_g$ for $\eta = 4$. Naturally the exact value of T_e and η cannot be determined out of this measurement.

Another point to be noted is the abrupt change in the rate at densities around 10^{16} m^{-3} (marked by a vertical line). Though the exact origin of this phenomenon is still unclear, the fact that this sudden transition from recombination dominated to diffusion dominated decay occurs at approximately the same densities regardless of the discharge conditions is remarkable. It should be noted that this transition occurs where the recombination rate becomes approximately equal to the diffusive loss rate which might be a starting point for further investigations.

B. Time and spectrally resolved emission

The highly excited states formed in the recombination process relax to lower levels through collisional quenching and spontaneous emission. For the higher lying levels the collisional quenching dominates, while for the lower levels the de-excitation through emission overtakes. Due to the strong dependence of both processes on the quantum number, the levels where the two processes give equal contribution exhibit the lowest net de-excitation rate. This is the so-called bottleneck [42] which limits the recombination. Its exact position depends on electron density and temperature and is represented by the factor η in Eq. (8). For the density range occurring in our experiments, the bottleneck appears for the levels characterized with quantum numbers p between 12 and 21, depending on the exact conditions as shown in Fig. 2. Then, the emission observed in the afterglow is expected to originate mostly from the states below the bottleneck.

Figure 8 shows the evolution of the spectra in the afterglow at 5 Pa and 1 kW rf power. The higher pressure is chosen since it provides a much better signal to noise ratio. For comparison, the steady-state spectrum in the same spectral range is also shown. Due to the decrease of the electron temperature all excitation processes are quickly extinguished leading to the observed disappearance of the emission immediately after power switch-off. At later times recombination populates the upper states and they start to cascade down which leads to reappearance of the emission. A comparison of the afterglow spectra with the spectrum under stationary conditions shows that the most intense lines in both cases originate from the transitions with upper states with quantum numbers $p = 5$ and $p = 6$. It is further observed that in the afterglow for $t > 500$ μs the relative line intensities and their ratios do not change. This indicates that the relative population of the upper states of the observed transitions is independent of the temporal change of the electron density and temperature.

A more striking—but expected—effect is that beside the emission lines present in the steady-state discharge, some additional lines emerge. These are for example the lines in the wavelength region between 470 and 515 nm. Figure 9 shows a comparison between the spectra in the stationary plasma and in the afterglow in this wavelength region. The spectrum for $t = 500$ μs is chosen but it is representative for all subsequent spectra. The vertical lines represent transitions of neutral argon atoms obtained from the NIST database [43]. The principle quantum number of the upper state of the transition is also shown next to the lines.

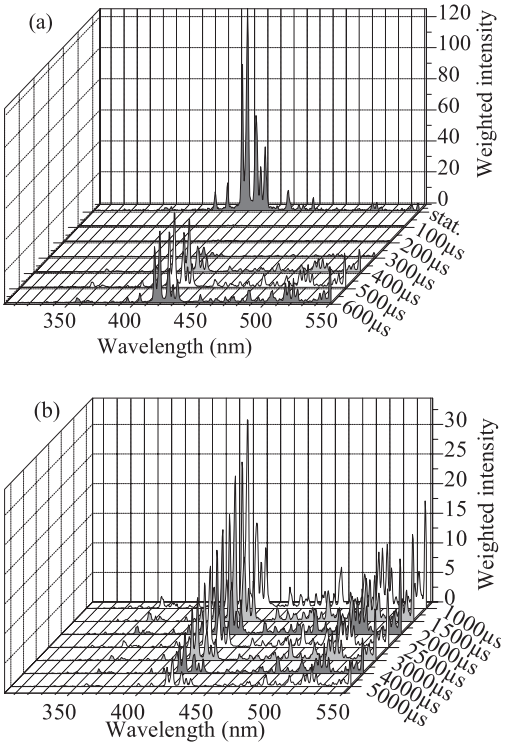

FIG. 8. Temporal evolution of the spectrally resolved emission intensity in the afterglow at $p = 5$ Pa and $P_{rf} = 1$ kW. In the first figure also the spectrum for the stationary discharge is shown. Note that the scales are different.

This reveals that the relatively strong afterglow line around 488 nm is most likely a superposition of several lines which could not be resolved with the spectrometer. These lines originate from states with principal quantum numbers between 7 and 11. The line with the highest quantum number is the line at 480 nm corresponding to $p = 12$ with an energy (15.66 eV) close to the ionization threshold (15.76 eV). The fact that such lines are present, indicates that the mean electron energy is much lower than the ionization energy of these states (0.1 eV). This is consistent with the picture of evaporative cooling of

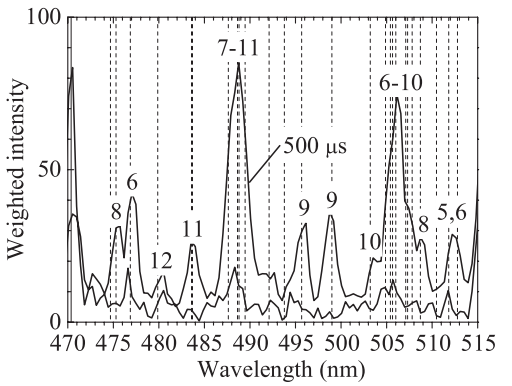

FIG. 9. Comparison of the argon spectra between 470 and 515 nm in the stationary plasma and in the afterglow. The vertical lines represent transitions from higher lying states. The numbers indicated next to the lines are the quantum numbers of the upper state of the transitions.

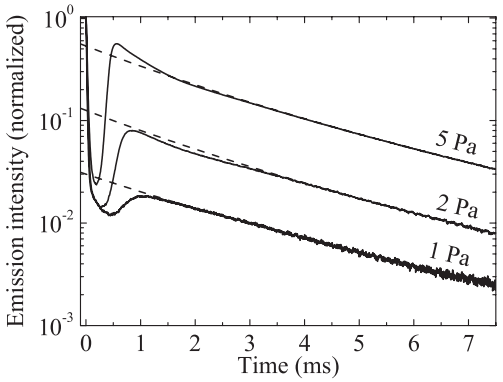

FIG. 10. Emission intensity between 413 and 423 nm measured at $P_{rf} = 1$ kW and various pressures. The intensity is normalized to its steady-state value. The dashed lines are fits according to Eq. (26). For the fit curve at 1 Pa only the absolute value is adjusted, the other parameters are the same as for the curve in Fig. 5.

electrons. In the case of the stationary discharge spectra, ionic transitions must be considered additionally since there the electron density and temperature are high. For example, the 488 nm line might originate from the prominent Ar^+ transition known from helicon discharges [44–46]. The lines around 484 and 499 nm only appear in the afterglow and are related to high lying states as shown in Fig. 9. The observed optical transitions originating from levels with quantum numbers up to $p = 12$ are consistent with the picture of the de-excitation bottleneck since at 5 Pa the electron density is higher and the bottleneck occurs at a state with a lower quantum number (Fig. 2).

The spectrum in a narrower spectral range between 413 and 423 nm recorded at different pressures is presented in Fig. 10. It is obvious from Fig. 8 that the strongest lines are in this wavelength range. These neutral lines correspond to the following transitions: the Ar $3p_6 \rightarrow 1s_5$ transition (in Paschen notation) at 415.8 nm, the $3p_1 \rightarrow 1s_5$ transition at 419.8 nm, and the $3p_9 \rightarrow 1s_5$ transition at 420.1 nm. The radiative lifetimes of the corresponding upper states of these three lines are all about 1 μs [43].

The initial decrease of the emission and its following increase are better visible in Fig. 10. The increase is up to 50% of the value in the stationary plasma. The time at which the maximum occurs varies with pressure and decrease from $t_{max} \approx 1000$ μs at 1 Pa over $t_{max} \approx 800$ μs at 2 Pa to $t_{max} \approx 500$ μs at 5 Pa. This behavior can be explained by enhanced recombination at the higher electron densities which shifts the maximum naturally to earlier times [Eq. (28)].

Noting that the registered intensity is proportional to the density of the radiative states, a comparison with Eq. (26) can be made. An amazing agreement is obtained. This agreement also provides indirect confirmation of the assumption for adiabatic change of the densities of both the Rydberg states and the radiative states. The deviations from the analytical formula around the peaks are probably due to violation of this assumption. The radiative de-excitation of these states leads to enhancement in the population of the metastable states.

C. Metastable density evolution

After the recombination and the subsequent de-excitation, the atoms end up either in the ground state or in one of the metastable states of the argon atoms, leading to an increase in their density. TDLAS is applied to measure the metastable density evolution in the afterglow. Figure 11(a) shows the temporal development of the absolute metastable density ($1s_5$) at 1 Pa and different powers. The values in the stationary discharge are given in Fig. 11(b). Figure 12 presents the obtained temporal variation of the normalized metastable density at an rf power of 1 kW and different gas pressures. Figures 11 and 12 show only mean densities since the absorption measurement performs a line integration. In the stationary discharge the metastable density is indeed distributed rather homogeneously [35]. However, when metastables are created by recombination a density profile close to the electron density distribution (Bessel function J_0) can be expected.

The evolution of the metastable density in the afterglow—as opposed to that in the stationary discharge [35]—is determined by a number of different processes as depicted in Fig. 1. These leave a specific fingerprint that can be identified in the observed temporal development. Immediately after pulse termination the metastable density decreases mostly due to quenching by electrons, the diffusional losses occur on a much longer time scale. A comparison of the different collisional rates [47] reveals that it is mostly excitation to the neighboring Ar $1s_4$ resonance state followed by radiative decay to the ground state

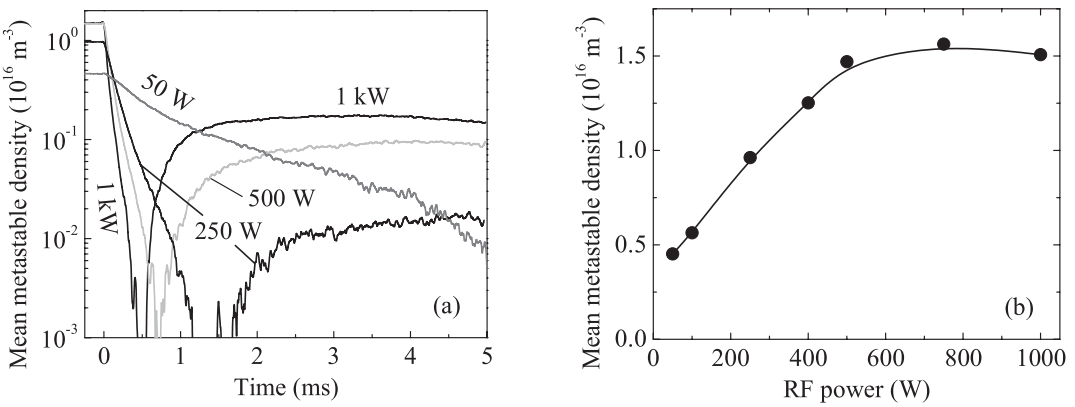

FIG. 11. Temporal evolution of the metastable density at 1 Pa and different rf powers (a) and variation of the metastable density with the rf power in the steady state (b). The line in (b) is only a guide to the eye.

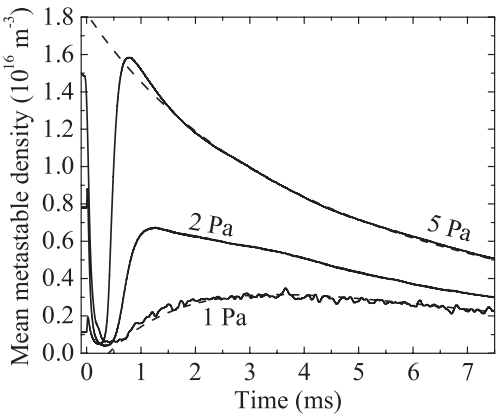

FIG. 12. Temporal evolution of the metastable density in the afterglow as a function of the pressure at $P_{rf} = 1$ kW. A fit according to Eq. (28) is superimposed on the data for 1 Pa and according to Eq. (29) to the data at 5 Pa.

that contribute to the loss of the metastable atoms. Since the quenching rate is proportional to the electron concentration, information about the steady-state electron density could be extracted from this initial phase [35]. Higher electron concentrations correspond to shorter quenching times and hence steeper decays. This is well illustrated in Fig. 11(a) where the metastables at 1 kW are practically completely destroyed within the first 500 μs of the afterglow, while at 50 W an appreciable amount of metastable atoms is still present even several milliseconds after the power has been switched off. The same trend can be recognized also in the curves at different pressures (Fig. 12). In this case a higher pressure corresponds to higher plasma densities and steeper decay.

At $t \approx 500$ μs the electrons are already cooled efficiently to values close to room temperature by evaporative cooling [7] which enhances recombination. Recombination produces highly excited states which then cascade down and start to populate the metastable states (cf. Fig. 1). This gives rise to the observed increase in their density and is described by the first term on the rhs in Eq. (24). Naturally, at lower rf powers and, respectively, lower electron densities recombination becomes negligible (cf. Fig. 7). Therefore, no increase of the metastable density is observed at lower powers [Fig. 11(a)].

At higher pressures the density of the ground state atoms is also higher making the optical transitions to them effectively less frequent due to the optical trapping of the radiation. This ultimately means that a bigger percentage of the excited atoms produced by recombination will end in the metastable states. As a result, the maximum density in the afterglow should increase with pressure compared to the value in the steady state (Fig. 12). This effect, in conjunction with the higher plasma densities (i.e., enhanced recombination), leads to an overshoot in the metastable density in the afterglow. At 5 Pa it is already a factor of 10 larger than the steady-state value. Furthermore, the absolute value of the steady-state metastable density decreases with pressure due to the decrease of the electron temperature.

At $p = 1$ Pa the afterglow metastable density is low and diffusion relatively strong. Therefore, Eq. (28) should provide a good description. In fact, the comparison is very satisfying throughout. Also the diffusion rate of 172 s^{-1} obtained from the fit is in excellent agreement with the literature value [48].

At higher pressures diffusion decreases. However, the obtained behavior clearly shows an increased decay rate. This increase is related to the increase in the metastable density formed in the afterglow. Metastables can now extinguish each other efficiently by energy pooling collisions. This behavior is represented by Eq. (29) which gives an excellent fit to the 5 Pa case. Due to the assumptions involved, however, this equation cannot describe the (short) rise of the metastables. The parameters obtained from the fit show that the pooling time constant is approximately equal to the diffusional time, which in this case amounts to about 10 ms. It has to be noted that this diffusional time is a factor of 3 shorter than one would expect from direct pressure correction of the diffusional rate at 1 Pa. This could be due to gas temperature effects or variation in the diffusion length resulting from different spatial profiles of the metastable density.

From the pooling time constant $\tau_p = 0.5/(k_m n_{max})$ an estimate for the maximal density n_{max} can be obtained. Using for k_m the value of 6.4×10^{-16} m^3/s [49], a value for n_{max} of 8.2×10^{16} m^{-3} is calculated. This agrees within a factor of 5 with the measured metastable density. The large factor cannot be a surprise as the rate calculation for energy pooling is only estimated by Ferreira *et al.* [49]. Given further inaccuracies resulting from the measurement (line integration) and from the diffusion rate, in fact, the agreement seems to be reasonable. The curve at 2 Pa shows a more complicated transition behavior where none of the simplifying assumptions in the analytical calculations can be justified.

V. CONCLUSION

In summary, a comprehensive and consistent picture of the recombination process in the low-pressure argon post-discharge is presented. A new recombination formula is proposed which considers both Stark splitting by ionic microfields and re-ionization by thermal electrons. This formula is combined with the effects of evaporative cooling and Coulomb collision, which allows the evolution of the electron density to be fully reproduced. Using the density evolution obtained in this way, further analytical models for the dynamics of the Rydberg atoms, the radiative excited states, and the metastable states are developed. The predictions of the models are compared with experimental data and very good agreement is found throughout.

Our results strongly support the following picture of the processes taking place in the afterglow: after the power is cut, the electrons lose energy by evaporative cooling and the existing metastable states are quenched. When the electron temperature reaches the gas temperature, the recombination sets in. This process populates the Rydberg states which decay down by quenching by the electrons to radiative states. The Rydberg states and the radiative states are separated by the so-called bottleneck. Furthermore, the de-excitation continues by spontaneous emission which ultimately leads to repopulation of the metastable states. At lower pressures these atoms are lost mainly by the slow diffusional process while at higher pressures energy pooling starts to play a role too.

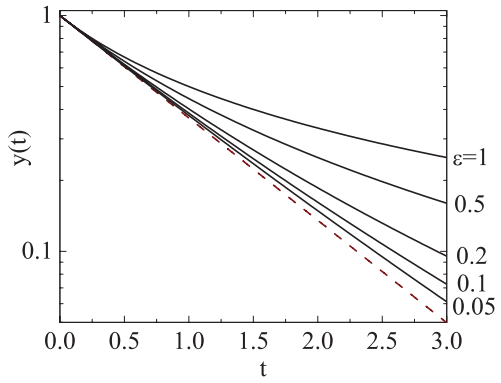

FIG. 13. (Color online) Plot of the solution of Eq. (A2) for various values of the parameter ϵ. The dashed line is the exponential function which is the limiting case for $\epsilon \to 0$. The vertical axis covers the range of normalized densities from Fig. 5 ($\epsilon = 0.2$) where the recombination dominates.

This effectively leads to a faster loss of metastable atoms as compared to the lower pressures.

An open challenge is the measurement of electron temperatures below the gas temperature. Furthermore, a direct measurement of the Rydberg states populated in the recombination process is highly desirable. Last but not least, the observed surprisingly sudden transition from recombination to diffusion poses an interesting question about the physical cause.

ACKNOWLEDGMENTS

The authors are thankful for the support of the Research Department Plasma and the DFG Research School of the Ruhr-University Bochum. The support from Nagoya University is as well gratefully acknowledged. Ts.V.Ts. would like to show his gratitude to the Alexander-von-Humboldt foundation for financial support. The authors are indebted to J. Winter and M. Böke for lending the microwave interferometer. S.Y. would like to thank the Graduate University for Advanced Studies (SOKENDAI) for supporting overseas travel expense. The authors would like to thank R. Johnsen and N. Sadeghi for fruitful discussions. Furthermore, we thank T. Zierow, F. Kremer, B. Becker, and S. Wietholt for the expert technical assistance.

APPENDIX

The essential point in the scaling of the recombination rate with the density according to Eq. (17) is that the dependence is rather weak: $\nu_r \propto n_e^{\epsilon}$, with $\epsilon = 2 - (9/2)\kappa \ll 1$, where $T_e \propto n_e^{\kappa}$. In the theory presented in the theoretical section ϵ varies between $1/5$ and $2/3$. The differential equation for the density evolution generally has the form

$$\dot{y} = -y^{1+\epsilon}. \tag{A1}$$

In this equation $y(t) = n_e(t)/n_e(t=0)$ is the density normalized to its initial value and the time has been normalized to a characteristic time constant $\tau^{-1} = \rho n_e(t=0)^{\epsilon}$. The solution with the initial condition $y(t=0) = 1$ is

$$y(t) = \frac{1}{(1+\epsilon t)^{1/\epsilon}}. \tag{A2}$$

This function has the property that in the limit $\epsilon \to 0$ it converges to $\exp(-t)$. For small but finite values of ϵ the solution deviates from an exponential function. However, the form is not very sensitive to the actual value of ϵ as long as $\epsilon \ll 1$. An example of the solutions for different values of ϵ is shown in Fig. 13.

The value of $\epsilon = 0.2$ derived in the theoretical section provides a very good fit to the experimental data. Nevertheless, from the above discussion a variation of this value by about $\Delta\epsilon/\epsilon = \pm 0.3$ would be difficult to identify. However, for κ the uncertainty is much smaller:

$$\frac{\Delta\kappa}{\kappa} = \frac{2}{9}\frac{\epsilon}{\kappa}\frac{\Delta\epsilon}{\epsilon} = \frac{1}{9}\frac{\Delta\epsilon}{\epsilon} = \pm 0.033. \tag{A3}$$

Therefore, the basic physical principal is well identified. In order to achieve a precise determination of the parameter time-resolved measurements of the electron temperature in the 10 meV regime would be necessary, which seems to be a real challenge.

[1] M. A. Biondi, Phys. Rev. **93**, 1136 (1954).
[2] R. R. Arslanbekov and A. A. Kudryavtsev, Phys. Rev. E **58**, 7785 (1998).
[3] R. R. Arslanbekov, A. A. Kudryavtsev, and L. D. Tsendin, Phys. Rev. E **64**, 016401 (2001).
[4] V. I. Kolobov and R. R. Arslanbekov, IEEE Trans. Plasma Sci. **34**, 895 (2006).
[5] A. Maresca, K. Orlov, and U. Kortshagen, Phys. Rev. E **65**, 056405 (2002).
[6] V. A. Godyak and V. I. Demidov, J. Phys. D: Appl. Phys. **44**, 233001 (2011).
[7] Y. Celik, Ts. V. Tsankov, M. Aramaki, S. Yoshimura, D. Luggenhölscher, and U. Czarnetzki, Phys. Rev. E **85**, 046407 (2012).
[8] G. P. Jackson and F. L. King, Spectrochim. Acta Part B **58**, 1417 (2003).
[9] J. A. Klingler, C. M. Barshick, and W. W. Harrison, Anal. Chem. **63**, 2571 (1991).
[10] L. Li, J. Robertson-Honecker, V. Vaghela, and F. L. King, Spectrochim. Acta Part B **61**, 722 (2006).
[11] X. Yan, Y. Lin, R. Huang, W. Hang, and W. W. Harrison, J. Anal. At. Spectrom. **25**, 543 (2010).
[12] M. A. Lieberman and A. J. Lichtenberg, *Principles of Plasma Discharges and Materials Processing* (Wiley, Hoboken, NJ, 2005).
[13] J. J. Thomson, Philos. Mag. **47**, 337 (1924).
[14] D. R. Bates, A. E. Kingston, and R. W. P. McWhirter, Proc. R. Soc. London Ser. A **267**, 297 (1962).

[15] D. R. Bates, A. E. Kingston, and R. W. P. McWhirter, Proc. R. Soc. London Ser. A **270**, 155 (1962).
[16] J. Stevefelt, J. Boulmer, and J.-F. Delpech, Phys. Rev. A **12**, 1246 (1975).
[17] T. Pohl, D. Vrinceanu, and H. R. Sadeghpour, Phys. Rev. Lett. **100**, 223201 (2008).
[18] Y. Hahn, Phys. Lett. A **231**, 82 (1997).
[19] T. C. Killian, M. J. Lim, S. Kulin, R. Dumke, S. D. Bergeson, and S. L. Rolston, Phys. Rev. Lett. **86**, 3759 (2001).
[20] R. A. Johnson, B. T. McClure, and R. B. Holt, Phys. Rev. **80**, 376 (1950).
[21] M. Tadokoro, H. Hirata, N. Nakano, Z. L. Petrović, and T. Makabe, Phys. Rev. E **58**, 7823 (1998).
[22] K. Hioki, H. Hirata, S. Matsumura, Z. L. Petrović, and T. Makabe, J. Vac. Sci. Technol. A **18**, 864 (2000).
[23] G. A. Hebner and P. A. Miller, J. Appl. Phys. **87**, 8304 (2000).
[24] G. Nersisyan, T. Morrow, and W. G. Graham, Appl. Phys. Lett. **85**, 1487 (2004).
[25] N. Nafarizal, N. Takada, and K. Sasaki, J. Phys. D: Appl. Phys. **41**, 035206 (2008).
[26] L. J. Overzet and J. Kleber, Plasma Sources Sci. Technol. **7**, 512 (1998).
[27] M. Osiac, T. Schwarz-Selinger, D. O'Connell, B. Heil, Z. L. Petrović, M. M. Turner, T. Gans, and U. Czarnetzki, Plasma Sources Sci. Technol. **16**, 355 (2007).
[28] S. Mohr, B. Du, D. Luggenhölscher, and U. Czarnetzki, J. Phys. D: Appl. Phys. **43**, 295201 (2010).
[29] J. J. Thomson, Philos. Mag. **23**, 449 (1912).
[30] Y. Hahn, Rep. Prog. Phys. **60**, 691 (1997).
[31] M. J. Seaton, Rep. Prog. Phys. **46**, 167 (1983).
[32] M. Yu. Romanovsky and W. Ebeling, Contrib. Plasma Phys. **46**, 295 (2006).
[33] D. R. Inglis and E. Teller, Astrophys. J. **90**, 439 (1939).
[34] A. V. Mitrofanov, Sov. Astron.–AJ **16**, 867 (1973), http://articles.adsabs.harvard.edu/cgi-bin/nph-iarticle_query?bibcode=1973SvA....16..867M&db_key=AST&page_ind=0&plate_select=NO&data_type=GIF&type=SCREEN_GIF&classic=YES.
[35] Y. Celik, M. Aramaki, D. Luggenhölscher, and U. Czarnetzki, Plasma Sources Sci. Technol. **20**, 015022 (2011).
[36] H. A. Bethe and E. E. Salpeter, *Quantum Mechanics of One- and Two-Electron Atoms*, 2nd ed. (Plenum, New York, 1977).
[37] L. Vriens and A. H. M. Smeets, Phys. Rev. A **22**, 940 (1980).
[38] T. Gans, D. L. Crintea, D. O'Connell, and U. Czarnetzki, J. Phys. D: Appl. Phys. **40**, 4508 (2007).
[39] A. Brockhaus, G. F. Leu, V. Selenin, Kh. Tarnev, and J. Engemann, Plasma Sources Sci. Technol. **15**, 171 (2006).
[40] Ts. Tsankov and Zh. Kiss'ovski, in *Meetings in Physics at University of Sofia*, edited by A. Proykova (Heron, Sofia, 2005), Vol. 6, pp. 38–42.
[41] L. Ricci, M. Weidemüller, T. Esslinger, A. Hemmerich, C. Zimmermann, V. Vuletic, W. König, and T. W. Hänsch, Opt. Commun. **117**, 541 (1995).
[42] S. Byron, R. C. Stabler, and P. I. Bortz, Phys. Rev. Lett. **8**, 376 (1962).
[43] "NIST database" (January 2012), http://www.nist.gov/pml/data/asd.cfm.
[44] P. Zhu and R. W. Boswell, Phys. Rev. Lett. **63**, 2805 (1989).
[45] I. D. Sudit and F. F. Chen, Plasma Sources Sci. Technol. **5**, 43 (1996).
[46] Y. Celik, D. L. Crintea, D. Luggenhölscher, U. Czarnetzki, T. Ishijima, and H. Sugai, Phys. Plasmas **18**, 022107 (2011).
[47] O. Zatsarinny and K. Bartschat, J. Phys. B **37**, 4693 (2004).
[48] F. Hutchinson, Phys. Rev. **72**, 1256 (1947).
[49] C. M. Ferreira, J. Loureiro, and A. Ricard, J. Appl. Phys. **57**, 82 (1985).